Chapter 8

Beam Rate Simulations

The ultimate goal of the beam delivery simulations is a complete "End-to-End" study from pion production on the target to stored muons in the ring. This goal will be achieved by using a sequence of specialized tools. They include a MARS calculation for pion production, G4Beamline and MAD8 calculations of the pion-to-muon decay line, the Delivery Ring, and the final beamline into the storage ring, a detailed GEANT4 and BMAD simulations of the transmission into the ring and the final storage fraction. This is ongoing work by many collaborators. In this chapter we present the status of the individual pieces, the results of Preliminary Design simulation studies of pion production, muon capture, beam transport and injection into the $(g-2)$ storage ring, and discuss future plans.

8.1 Pion Production at the Target

The description of the pion production target and lithium lens are given in Chapter 7. In this section we describe the software model of the target and lithium lens, give details of the simulations, summarize results and discuss future plans.

8.1.1 MARS Model and Beam Initial Conditions

Pion production in the target and focusing of the secondary beam by the lithium lens were simulated using MARS [1]. A graphical representation of the MARS model of the target and the lens is shown in Fig. 8.1. The target consists of a 11.43-cm-diameter 25.4-cm-long Inconel cylinder (1) enclosed into a 6-mm-thick Be container (red ring in Fig. 8.1). The target is off-centered horizontally relative to the beam axis by 4.31 cm. The intersection of the beam with the Inconel cylinder is therefore about 7.5 cm long.

Secondary beam particles produced in target are focused by the lithium lens. The most relevant part for our simulations is the 16-cm-long 2-cm-diameter Li cylinder (2) with a 232 T/m focusing magnetic field produced by the electric current flowing along the axis of the cylinder. We assume ideal focusing field (i.e., no attempts have been made so far to model a more realistic or time-dependent field).

In Ref. [2] a study was done of the pion collection efficiency dependence on the focusing field and position of the lithium lens relative to the production target. As expected, stronger

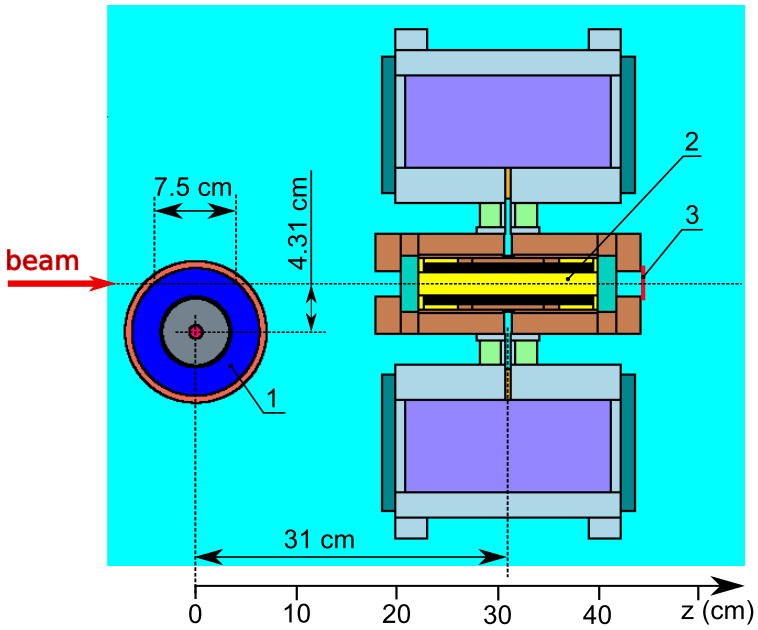

Figure 8.1: MARS model of the E989 target station (top view): Inconel target (1), 16-cm-long 2-cm-diameter Li cylinder with magnetic field (2), virtual detector, $z = 43$ cm (3).

focusing fields result in better pion collection.

For our final simulations we use the baseline design value of 232 T/m recommended by the experts. The chosen field strength results in high pion collection efficiency and allows for long-term reliable operation of the lithium lens at 12 Hz repetition rate in a pulsed mode with irregular time structure of the beam (see section 7.2). The position of the lithium lens with 232 T/m focusing field was also optimized for pion collection efficiency. The optimization was done by maximizing the number of pions inside a 40π mm-mrad acceptance ellipse at virtual detector (3) as seen in Fig. 8.1. Twiss parameters defining the phase-space ellipses were taken from the beamline lattice design in Ref. [3] ($\beta_x = 2.105$ m, $\alpha_x = 0.033$, $\beta_y = 2.274$ m, $\alpha_y = 0.001$). The pion momentum range was limited to a 2.7-3.5 GeV/c band. The simulated number of accepted pions per proton on target as function of lithium lens position is shown in Fig. 8.2. The highest number of pions was observed when the lithium lens is placed at $z = 31$ cm, which is within its operation range. In future, the position of the lithium lens can be refined to maximize the number of magic-momentum muons entering the $(g-2)$ storage ring.

The primary proton beam with 0.3π-mm-mrad emittance has a kinetic energy of 8 GeV. As it was shown in Ref. [4] and also seen in Fig. 8.2, smaller proton beam sizes lead to higher pion fluxes within the beamline admittance. According to the baseline design, the size of the primary proton beam on target will be 0.15 mm (see Section 7.4.1). For our baseline calculations we assumed Gaussian proton beam with $\sigma_x = \sigma_y = 0.15$ mm spot size at $z = 0$ and $\sigma_{x'} = \sigma_{y'} = 2$ mrad angular divergence[1].

The physics information (momentum, coordinates, spin, etc.) of beam particles entering

[1]The specified size of the beam spot at $z = 0$ is assumed in the absence of the target. Multiple scattering in the target material slightly broadens the primary beam.

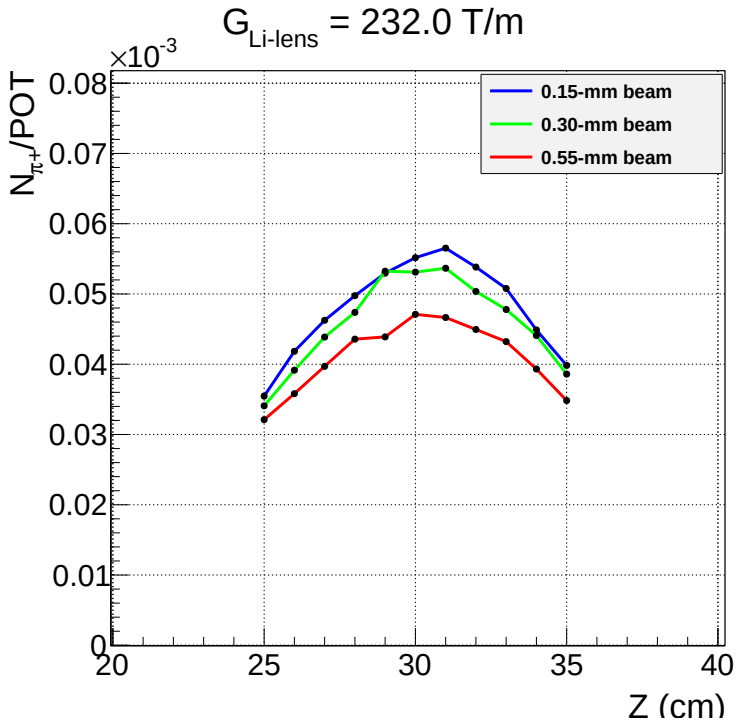

Figure 8.2: Number of pions at the downstream face of the lithium lens within 40π mm-mrad acceptance ellipse ($\beta_x = 2.105$ m, $\alpha_x = 0.033$, $\beta_y = 2.274$ m, $\alpha_y = 0.001$) as function of lithium lens position relative to the production target (center-to-center). Software cut on pion momentum was limited to $\pm 2.5\%$ around magic momentum. Three lines correspond to three different spot sizes of the proton beam as indicated in the insert.

the virtual detector (3) with $|x|, |y| < 20$ mm, $|x'|, |y'| < 20$ mrad and $2.7 \leq p \leq 8.0$ GeV/c were recorded for the second simulation step using the `G4beamline` program. Thus, the phase space of recorded particle was chosen to be larger than the admittance of the beamline so as to not introduce any bias.

8.1.2 Polarization of Muons off the Target

Magic-momentum muons originate from in-flight decays of pions with momenta in the range from 3.1 to 5.3 GeV/c. The longitudinal polarization dependence (along pion momentum) and emission angle (relative to pion momentum) of magic-momentum muons as a function of pion momentum are shown in Fig. 8.3. In the pion decay channel, the momentum distribution of pions is relatively narrow, $\Delta p_\pi / p_{\text{magic}} \approx \pm 10\%$, producing highly-polarized magic-momentum muons. In contrast, the momentum distribution of pions in the target station is very broad, resulting in magic-momentum muons originate with a wide range of polarizations.

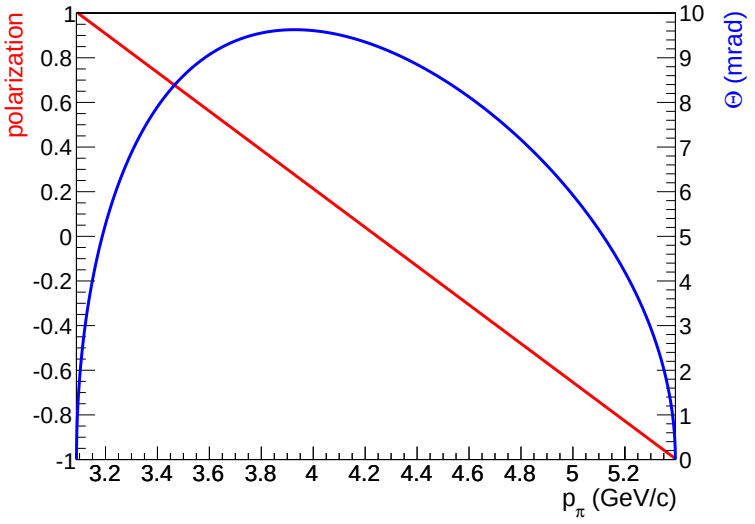

Figure 8.3: Horizontal polarization (red) or emission angle relative to pion momentum (blue) of magic-momentum muons as function of pion momentum. The components of muons polarization vector are plotted in a so-called *centerline* coordinate system where the Z axis is running down the center of the beamline, the X axis is beam left, and the Y axis is up.

The `MARS` simulation does not track polarization. Thus, we had to introduce spin tracking code into `MARS` ourselves. The distribution of horizontal components of polarization of magic-momentum muons ($\Delta p/p = \pm 0.5\%$) originating from pion decays upstream to virtual detector (3) (see Fig. 8.1) is shown in Fig. 8.4. The average polarization of these muons is about 0.55.

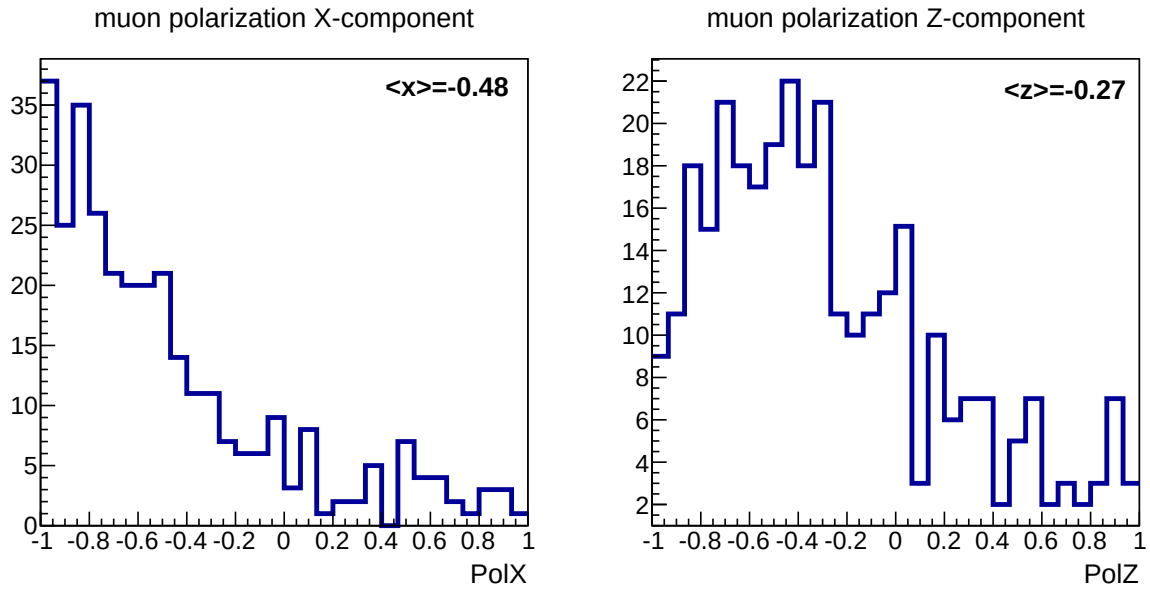

Figure 8.4: Horizontal components of polarization of magic-momentum muons ($\Delta p/p = \pm 0.5\%$).

8.2 Target–to–Storage-Ring Transport

Simulation of pion beam transport starting from virtual detector (3) (See Fig. 8.1), including pion decay and muon capture, and muon beam transport to the $(g-2)$ storage ring was performed using `G4beamline` program. In this section we present the `G4beamline` model of the beamline, describe difficulties we encountered in the process of building a software model of the beamline, present the results of simulations and discuss future plans.

8.2.1 `G4Beamline` Model and Optics Validation

`G4Beamline` is a particle tracking and simulation program based on the `GEANT4` toolkit. `GEANT4` was originally conceived for modeling detectors; `G4Beamline` extends `GEANT4` simulations to beamline elements, beam transport lines and decay beam lines. Concretely this means that `G4Beamline` provides standard beamline elements defined in terms of `GEANT4` primitives. In addition, it allows the user to work in beam coordinates, either to specify beamline geometry or to analyze and interpret tracking results. Note that all trajectory integrations are ultimately performed in absolute coordinates using time as the integration variable by `GEANT4`. This also implies that it is as accurate and realistic as the `GEANT4` toolkit implements.

`G4Beamline` allows simulation of important aspects of the $(g-2)$ experiment in an integrated manner, including muon production in the decay line, muon capture by the beamline and muon transport to the $(g-2)$ ring. Most importantly, in combination with the simulation program `gm2RingSim` – which is also based on `GEANT4` – the impact of beam-related systematic errors can be studied.

The $(g-2)$ delivery beamlines are designed using the standard optics code `MAD8`. Like

virtually all beam optics codes, MAD8 does not have an explicit notion of three-dimensional space. Rather, a beamline is represented as an ordered sequence of elements which in turn, uniquely defines a design trajectory. Since the trajectory of a particle through a magnet depends on its initial conditions at the magnet input face, *a-priori* assumptions about the latter must be made. For all focusing elements, MAD8 assumes that the trajectory is a straight line entering and exiting at $(x = 0, x' = 0, y = 0, y' = 0)$ in the element local transverse coordinate system. For bending elements it is assumed that the particle entrance and exit angles are of equal magnitudes and opposite signs. In the case of an ideal sector magnet (SBEND) the entrance and exit angles with respect to the magnet faces are trivially zero. For a rectangular bend (RBEND) these angles are equal to $\theta/2$, θ being the net bending angle through the magnet.

The G4Beamline models of the delivery lines are constructed by direct translation of the design lattice in MAD8 format (Fig. 8.5). To maximize translation reliability, the latter is performed in an automated manner, using a program written specifically for that purpose.

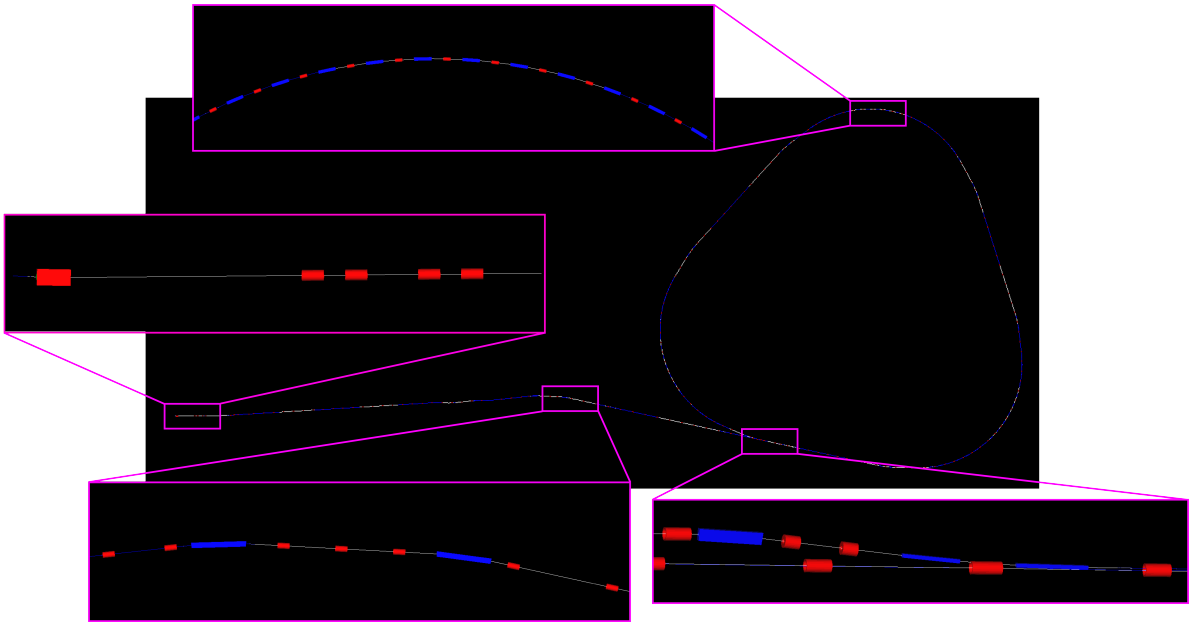

Figure 8.5: G4Beamline model of the *M2-M3-delivery ring* section of the $(g-2)$ delivery beamline.

Early on, a number of deficiencies in G4Beamline were identified. In collaboration with the code developer (who has been responsive to our needs and concerns), appropriate fixes were developed and incorporated into G4Beamline official releases.

Even though G4Beamline has been used with success by a number of groups, the code had never been exercised much or at all to model moderately complex non-planar lattices. Thus, when the absolute positions of the G4Beamline magnets were compared to the 3-dimensional site coordinates produced with the MAD8 survey command, some small but nevertheless noticeable discrepancies were observed.

We ultimately identified and addressed a number of issues

1. Rectangular bend magnets were effectively always rotated in space with respect to a

point located in the center of the magnet. To replicate MAD8 positioning, such magnets need to be rotated by half the net bend angle with respect to an axis passing through the origin of the upstream face. Note in passing this issue adversely affected the geometric acceptance.

2. The beam reference coordinate system was not transformed properly in rotated bending dipole magnets, resulting in incorrect transverse beam coordinates.

3. The polarization state was ignored when saving or reading a particle distribution. A related issue was that it was not possible to read an arbitrary initial polarization distribution. Uniform polarization was the initial condition supported by the program.

4. N being the number of elements in the lattice, we observed an $O(N^2)$ scaling of the time required to integrate trajectories. The inefficiency was traced to the technique used to determine, at each time step, the position of a particle in local element coordinates for purpose of evaluating the local electromagnetic field. After discussions, an improved algorithm based on voxelization techniques was developed and implemented by the code author. Near $O(N)$ scaling is now achieved.

G4Beamline still has shortcomings (as of time of this writing) that are relevant to our simulations.

- it generally does not efficiently handle accurate integration through sharp-edged fields. This issue principally affects idealized bending elements where the magnetic field exhibits an abrupt jump at the upstream and downstream faces. The immediate effect is a small error on the particle angle which translates into a noticeable position error further downstream. To perform accurate numerical integration, the integrator needs to precisely anticipate the time at which a particle will cross a magnet face boundary. In practice, this turns out not to be an easy problem to deal with and the best strategy often ends up being the imposition of a relatively small limit on the maximum allowed step size. While the integration accuracy is improved, the cost in terms of computational efficiency tends to be high.

- G4Beamline does not correctly handle dipole edge focusing. This usually results in the introduction of a modest amount of beam envelope modulation which may affect the accuracy of computed acceptance. Work on a fix for this issue is on-going. Note that in principle, edge focusing effects are completely accounted for when a detailed fringe field description can be included. Currently this is supported only for rectangular bends with poles faces at nominal orientation.

G4Beamline offers two methods to position elements: (1) the sequential method where the position of each element is expressed relatively in a local coordinate system referred to as centerline coordinates, and (2) the absolute method where each element is positioned absolutely in a fixed global coordinate system. Since the sequential method most closely follows the default mode of operation of an optics code, we have relied on this approach to produce our initial G4Beamline geometry models.

While very convenient, the sequential technique of positioning beamline elements lacks generality. This is due to the implicit assumption that the design trajectory through each element is uniquely defined. This is not always the case for a number of reasons, including :

- Some elements are time-dependent e.g. kicker magnets.
- Some magnets are positioned in such a way that the design trajectory traverses them more than once. For example, to relax the requirements on the time-dependent kicker, the beam injected into the delivery ring enters at an offset through ring quadrupoles before being kicked to become tangential to the ring central ring orbit.

To simulate the entire $(g-2)$ beam transport process including transport to and injection into the delivery ring followed by extraction after a few turns it became necessary to split the simulation into a few steps. A distinct beamline model is constructed for each step and the input particle distribution is assumed to be the output from the previous step. Using this approach, kickers can be modeled as (different) time-independent devices while quadrupoles where the beam nominal trajectory is off-center can be represented by combined function bends.

To confirm that the `G4Beamline` geometry is equivalent to `MAD8`, a number of sanity checks are performed.

- For both models the path lengths measured along the design trajectories (as reported by each code) should be in agreement at the mm level.
- The current version of `G4Beamline` generates an output equivalent to that of the `MAD8 survey` (i.e. the absolute positions of the center of the aperture at the entrance and exit faces of every element, in absolute coordinates). For a correct translation, all these positions should agree at the mm level.
- Finally, an appropriately matched particle distribution is tracked through the `G4beamline` model. The lattice functions are then extracted from the beam size and emittances and compared to the output generated by the `MAD8 TWISS` command.

For future simulations, we intend to use a single absolute coordinate model of the entire $(g-2)$ delivery line (M2-M3-delivery-ring-M4-M5) geometry. This will eliminate the bookkeeping involved in breaking a simulation into multiple steps and allow the use of truly time dependent kicker elements. We should point out that an automated procedure to generate such an absolute description directly from a collection of `MAD8` optics files has recently been developed. In this case, while the other checks remain useful, there is obviously be no need to compare the absolute position of the elements with that of the `MAD8 survey` command. On the other hand, absolute positioning introduces some additional complexity mainly related ascertain that both the field and element orientations reported by the `MAD8 survey` are correctly translated into equivalent `G4Beamline` element rotations.

8.2.2 Beam Transmission

To record the beam particles for offline analysis we installed several virtual detectors in the G4beamline model: a START detector at $z = 5$ mm downstream to the lithium lens; virtual detector VD5 in the injection region in the Delivery Ring (DR); virtual detector DRR in the DR near the point where the beam completes one revolution around DR; virtual detector DRE near the extraction point from the DR; and STOP detector after the last magnet of the entire beamline. An example placement of these detectors is shown in Fig. 8.6.

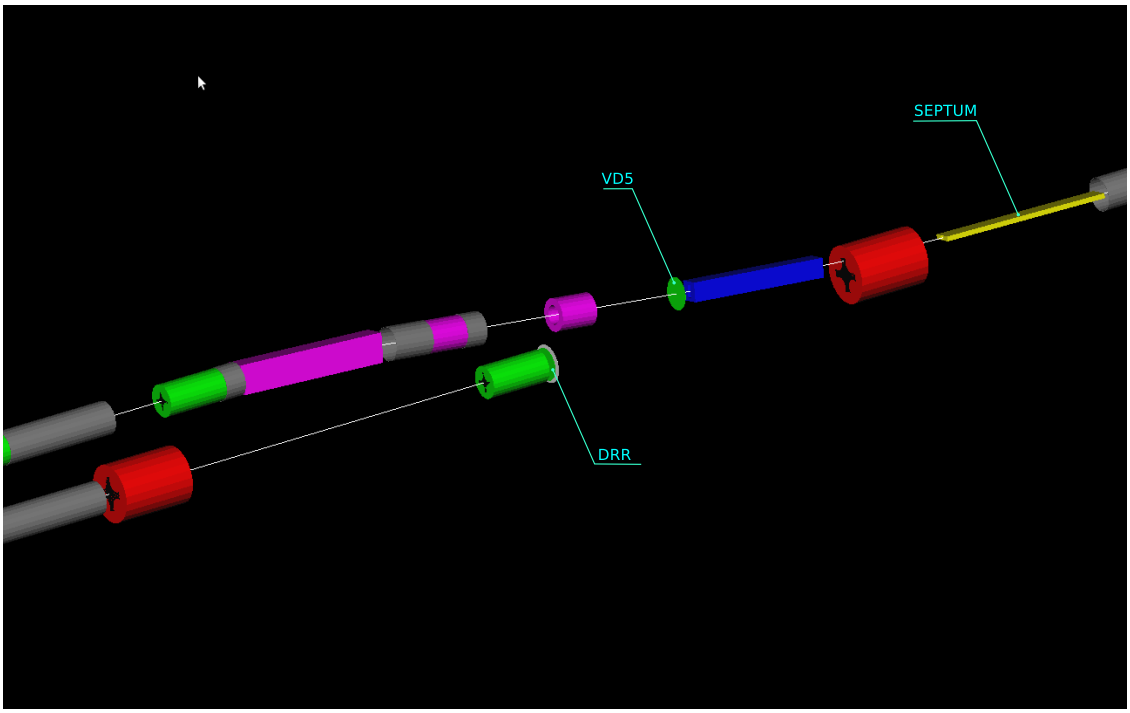

Figure 8.6: Location of virtual detectors near the injection point into the Delivery Ring in G4beamline model of the E989 beamline. VD5 is located near the point where the beam is injected into the Delivery Ring (DR); DRR is located near the point where the beam completes one revolution around the DR.

To study the transmission of the beam through the beamline, we disabled decays of unstable particle in the G4Beamline physics list. In such conditions a beam particle can be lost only if it hits a beamline element. In our simulations, only natural apertures of beamline elements determine the beam transmission, no additional software cuts have been applied.

The horizontal (x) and vertical (y) phase space distributions of particles in the START detector are shown in Fig. 8.7. The same distributions accumulated using only those particles which propagate all the way through the beamline into the STOP detector are shown in Fig. 8.8. Thus, the emittance of the transmittable pion beam is about 40π mm-mrad in agreement with the MAD design of the beamline.

The momentum distributions of pions in the three virtual detectors are shown in Fig. 8.9. We remind the reader that we used relaxed phase space cuts to select MARS data for tracking in G4beamline. Therefore, the number of hits in the START detector is relatively large. Due to magnet apertures only a fraction of the initial beam can be transmitted through the entire

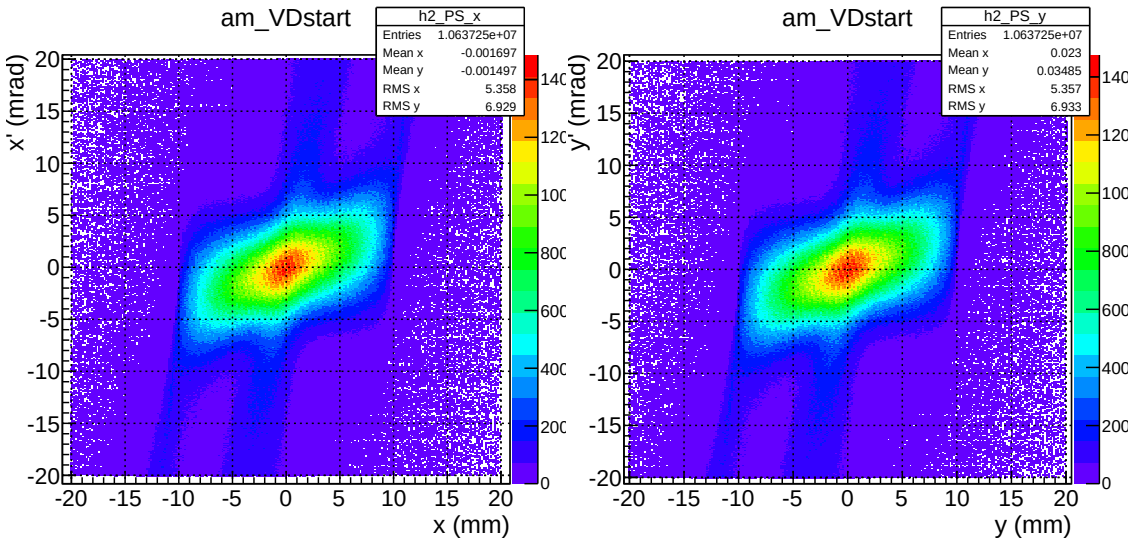

Figure 8.7: Horizontal (left) or vertical (right) phase space distributions of all particles in the START detector.

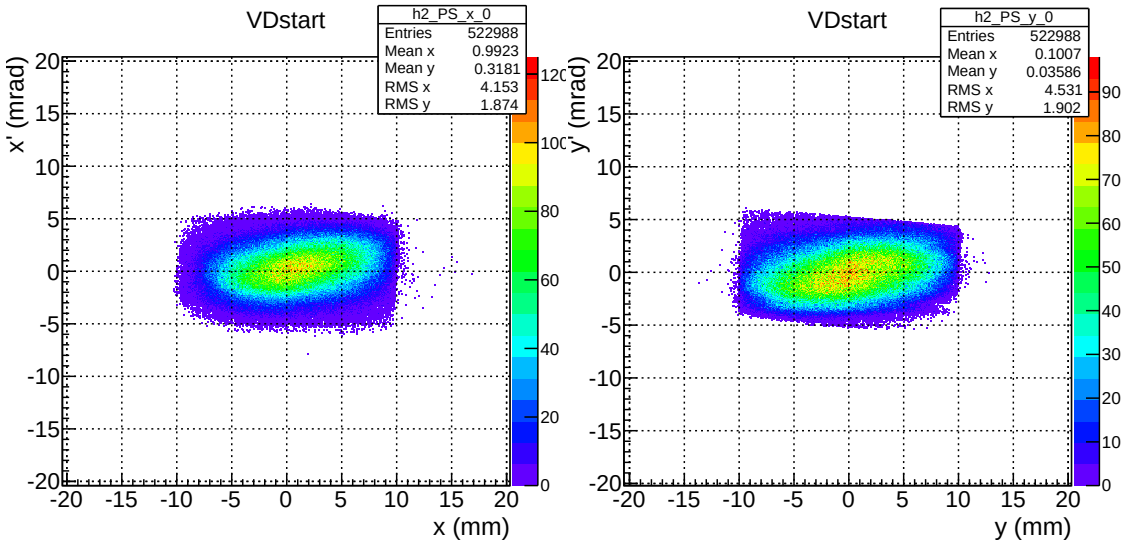

Figure 8.8: Horizontal (left) or vertical (right) phase space distributions in the START detector accumulated using only those pions which transmit through the entire beamline into the STOP detector. Decay of unstable particles disabled.

beamline. We also start with a relatively broad momentum cut (blue line). As discussed in the previous chapter, the initial momentum range is selected using the PMAG magnet. The width of the momentum distribution of the beam entering the DR is about 3.5% (RMS). The final momentum selection takes place in the DR as the last beamline section M4-M5 has no momentum-selecting elements. At the end of the beamline the width of the momentum distribution is about 1.2% (RMS).

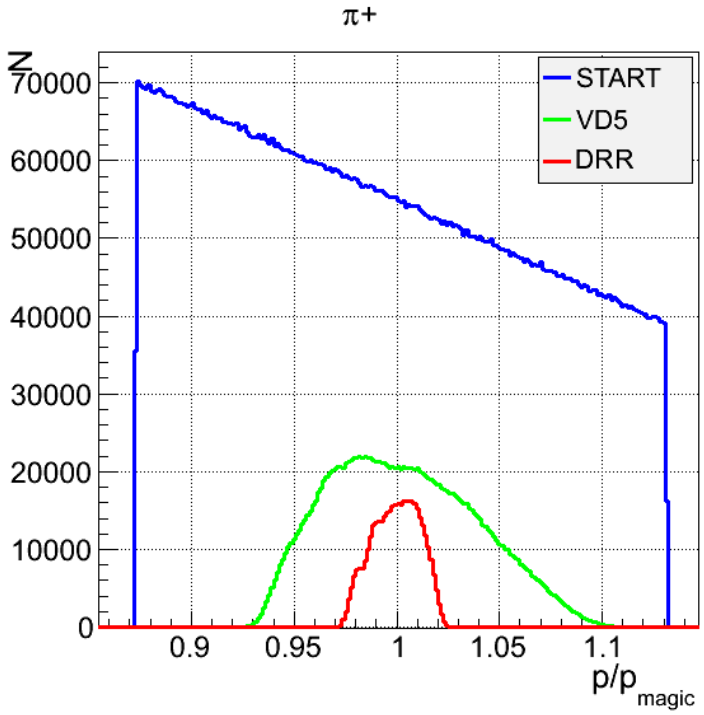

Figure 8.9: Momentum distribution of pions in START (blue), VD5 (green) and DRR (red) virtural detectors. Pion decay disabled.

8.2.3 Muon Collection

For the studies in this and the following sections we enable stochastic processes in G4beamline including decays of unstable particles. The momentum distributions of muons in virtual detectors START, VD5 and DRR are shown in Fig. 8.10. Sharp edges in the momentum distribution of muons in the START detector are due to a software cut of approximately 0.85-1.13 GeV/c applied to the MARS data to pre-select the relevant momentum range for tracking simulations. The momentum distribution of muons entering the DR (green histogram) has a complex shape because it includes muons originating before and after momentum-selecting beamline elements. After several revolutions in the DR almost all pions have decayed and the momentum distribution of muons resembles the distribution of beam particles in Fig. 8.9.

Since there is no momentum selection in the M4/M5 beamline section, the distribution of muon momenta at the end of the beamline (not shown in Fig. 8.10) has a similar shape to the one in the DRR detector. Currently, the design of the magnets for beam extraction from the DR has not been finalized yet, therefore in our model we assume 100% beam transmission

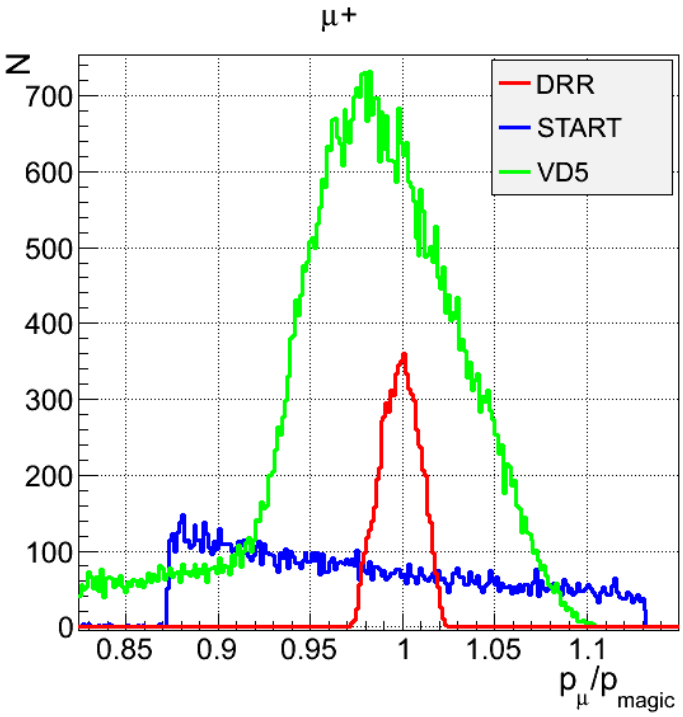

Figure 8.10: Momentum distribution of muons in `START` (blue), `VD5` (green), and `DRR` (red, after five turns around DR) virtural detectors.

through the apertures of magnets in the extraction optics. Therefore, the intensity of the muon beam reduces merely due to muon decays. Assuming three revolutions of the beam in the DR, the total number of magic-momentum muons ($\Delta p_\mu/p_{\rm magic} = \pm 0.5\%$) per proton on target at the downstream face of the last beamline magnet is 2.3×10^{-7}. However, as it will be discussed below, only a fraction of these muons will survive injection into the $(g-2)$ storage ring.

Using 1.2×10^{10} incident protons on target, `MARS` and `G4beamline` tracking simulations were performed to obtain a sample of about 10,000 muons in the `STOP` detector[2]. Physics parameters of these muons were recorded into an output file to be used as input for the studies of muon injection into the $(g-2)$ storage ring (see Section 8.3.1).

8.2.4 Beam Polarization and Distribution

The distribution of horizontal components (x and z) of the polarization of magic-momentum muons ($\Delta p/p = \pm 0.5\%$) in the `STOP` detector is shown in Fig. 8.11. The average polarization is approximately 95%. This includes approximately 5% of muons with low polarization origintating upstream of the `START` detector (see Fig. 8.4).

[2]For this we simulated three turns around the Debuncher Ring

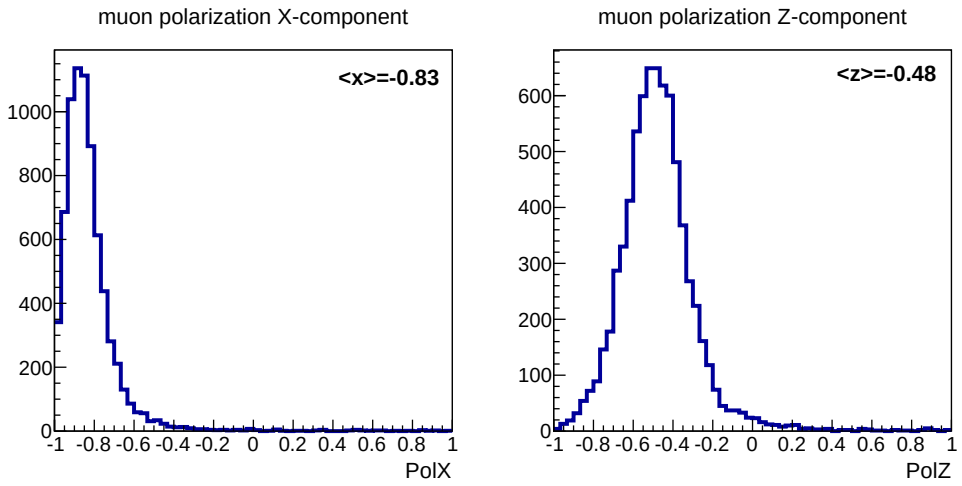

Figure 8.11: Horizontal components of polarization of magic-momentum muons ($\Delta p/p = \pm 0.5\%$) in the STOP detector.

8.2.5 Hadron Clean-up

The beam after the lithium lens is a mixture of mainly protons, neutrons and pions. The M2M3 beam line and Delivery Ring effectively selects all particles with a similar rigidity to the reference beam (predominantly protons and pions with momentum, $p \sim 3.1$ GeV/c) but the velocity difference between different species causes the mixed beam to separate into discrete populations. At the end of the M2M3 beamline, $\sim 82\%$ of the pions have decayed, so it is a mixed beam of mostly protons and muons that enters the Delivery Ring. After a number of turns round the Delivery Ring, the trailing proton beam can be extracted using the abort fast kicker. The rise-time of this kicker ($\sim$ 180 ns) determines the minimum gap required between the proton and muon beams to ensure a clean extraction of protons, without significant muon losses.

A MARS simulation of 10^9 protons on target was used to calculate the expected particle phase-space distribution at the end of the lithium lens. This gave $\sim 12.7 \times 10^6$ protons, $\sim 1.1 \times 10^6$ positive pions and a small number of muons ($\sim$ 3000) at the start of the M2 line. The longitudinal distribution of all particles was assumed to follow that of the incident proton beam. The MAD8 tracking code [6] was used to track protons and positive pions separately through the M2M3 line and for several turns round the Delivery Ring. In both cases the lattice was tuned to a nominal momentum of 3.1 GeV/c. The apertures within the lattice were modeled in a variety of ways. The apertures of the quadrupole star chambers have a complicated geometry (see Fig. 8.12) with different sizes used in the M2M3 beamline and in the Delivery Ring. Both types were approximated with a tilted square aperture with side length of 108 mm in the Delivery Ring and 84 mm in the M2M3 lines. The arc dipoles are modeled with a rectangular aperture with dimensions 128×60 mm^2. At the M2M3 merging location an off-set quadrupole (Q733) is used to impart a 25 mrad dipole kick. This was modeled within the MAD8 lattice by a bending dipole with a superimposed quadrupole field component. A similar technique is used to model the D3Q3 (injection) and D2Q5 (extraction) quadrupoles which impart a 30 mrad vertical kick to aid the transition

into and out of the Delivery Ring. All these quadrupoles are assigned circular apertures with a diameter of 200 mm.

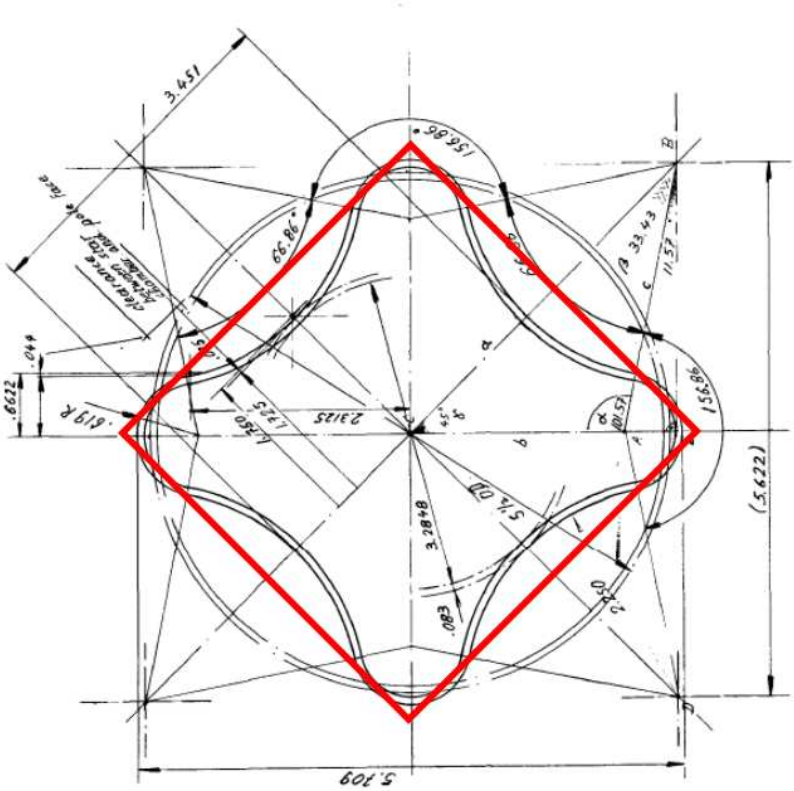

Figure 8.12: The approximation (red line) of the quadrupole star-chamber aperture used in the MAD8 model. The side length of the rectangular aperture was set to 108 mm for the quadrupoles in the Delivery Ring and 84 mm for those in the M2M3 beamline.

After tracking $\sim 12.7 \times 10^6$ protons from the end of the lithium lens, 113,930 survived to the middle of quadrupole Q202 in the Delivery Ring. The pions were also tracked from the beginning of the M2M3 line, with 90,038 surviving to the Delivery Ring. For these surviving pions, the probability of decay was calculated and a population of muons was randomly drawn from the parent pion population. The muon population was then tracked through the Delivery Ring. The separation between the beam centroids of the proton and muon populations was found to be 43.6 ns on injection to the Delivery Ring.

The populations of muons and protons were tracked separately round the Delivery Ring and their longitudinal distributions were calculated as a function of the number of turns. These longitudinal distributions are shown in Fig. 8.13 and the time interval between the two populations are summarised in Table 8.1. The rise time of the proton removal kicker magnets is ~ 180 ns, so a clean separation of the two populations can be achieved on the fourth turn. These results are in broad agreement with survival studies made with G4beamline and analytic calculations of the separation between the two particle bunches.

Approximately 35% of all particles were lost in the first turn (mainly in the quadrupole apertures in the arcs), with the particle losses dropping below 1%, for both species on

subsequent turns. The particle loss rates and a measure of the longitudinal distributions are summarised in Tables 8.2 (protons) and 8.3 (muons).

The work in this section has focused on modeling the M2M3/Delivery Ring lattice and the longitudinal distributions of the proton and muon populations. Future work will be concerned with a careful calculation of the absolute number of muons (and their distribution in phase-space) that are extracted from the Delivery Ring. It is expected that the current `MAD8` model will need improving to achieve this – in particular:

- The momentum deviation (from the reference 3.1 GeV/c) of some particles at the beginning of the M2M3 line is very large, which raises the question of how accurately the `MAD8` tracking model describes the motion of these particles. Modelling the lattice in other codes (`BMAD`, `PTC`) will enable the `MAD8` tracking to be benchmarked.

- The quadrupole apertures are described as rectangles rather than using an accurate description. Changing the aperture size in `MAD8` to intentionally under or overestimate the true aperture suggests that this approximation is reasonably good, but it may be useful to use a code that can realistically model the true aperture shape.

- The decay of pions to muons was approximated and was forced to occur at the entrance or exit of a lattice element, so the decay step length was no greater than the betatron wavelength. It is planned to implement an exact model of the decay dynamics, with the decay step length reduced to a distance much smaller than the betatron wavelength.

- It is planned to include muon spin tracking in the Delivery Ring simulations.

- All pions should be used in the decay calculation, rather than just the pions that survive at the end of the M2M3 line.

- The injection/proton separation/extraction kickers more will be modelled in more detail to better determine the number of muons delivered to the storage ring.

	Centroid time difference	Gap size
Injection	43.6 ns	None
1st turn at abort	94.6 ns	None
2nd turn at abort	169.1 ns	36.1 ns
3rd turn at abort	243.6 ns	108.4 ns
4th turn at abort	318.1 ns	180.3 ns
5th turn at abort	392.6 ns	252.2 ns
6th turn at abort	467.1 ns	324.1 ns

Table 8.1: Separation between protons and muons in the Delivery Ring.

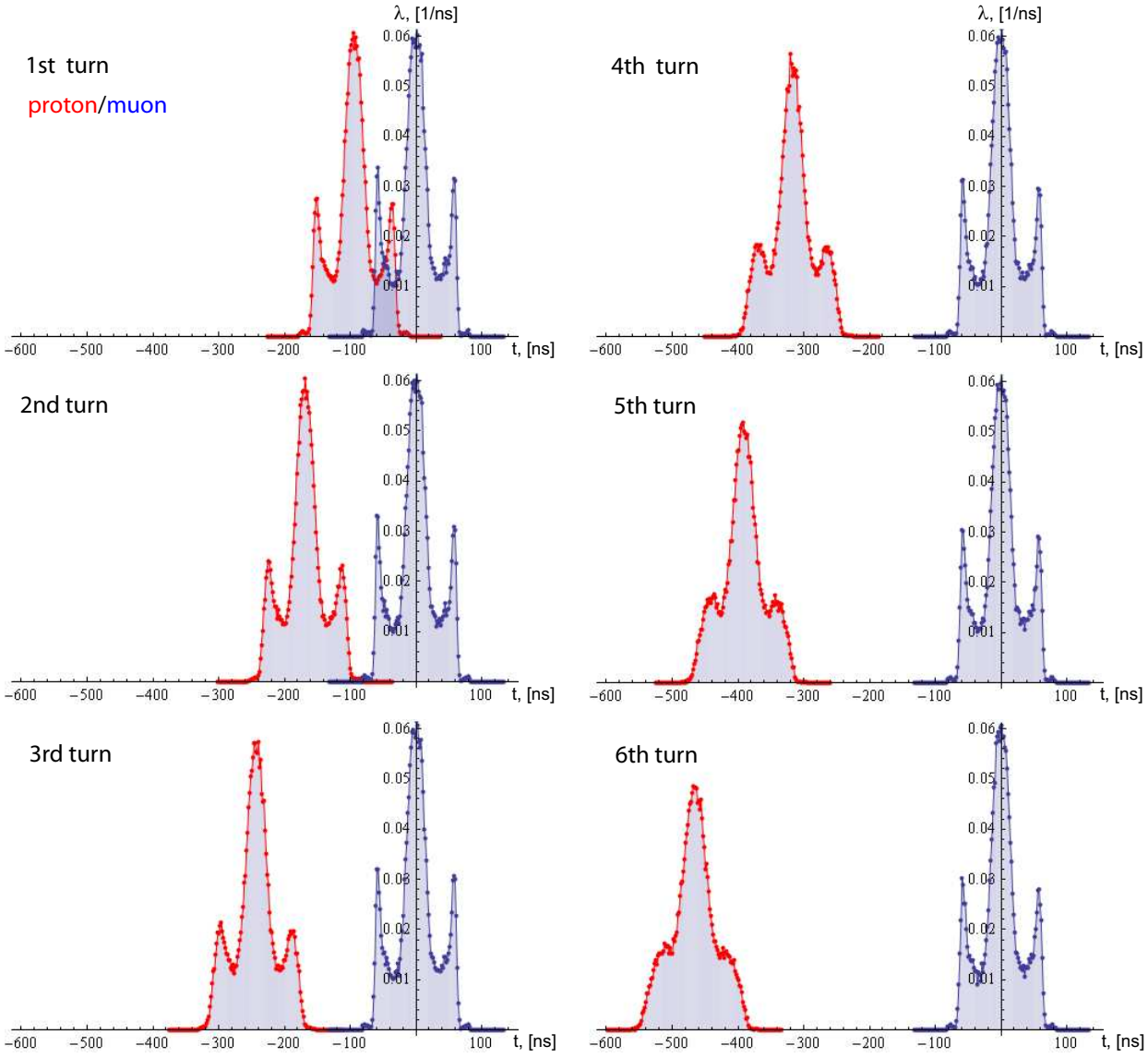

Figure 8.13: The normalised longitudinal distribution of the proton and muon populations as a function of turn number in the Delivery Ring

	Particle loss per turn	95% of protons within	99% of protons within	RMS $\Delta p/p$
1st turn	36.80 %	± 60.8 ns	± 66.5 ns	0.01390
2nd turn	0.78 %	± 61.7 ns	± 68.6 ns	0.01381
3rd turn	0.31 %	± 63.0 ns	± 70.6 ns	0.01377
4th turn	0.35 %	± 64.2 ns	± 72.8 ns	0.01374
5th turn	0.26 %	± 65.6 ns	± 75.0 ns	0.01371
6th turn	0.23 %	± 67.2 ns	± 77.2 ns	0.01368

Table 8.2: Proton longitudinal distribution in the Delivery Ring

	Particle loss per turn	95% of muons within	99% of muons within	RMS $\Delta p/p$
1st turn	35.12 %	± 60.1 ns	± 64.2 ns	0.01457
2nd turn	0.75 %	± 60.1 ns	± 64.4 ns	0.01447
3rd turn	0.31 %	± 60.2 ns	± 64.6 ns	0.01443
4th turn	0.31 %	± 60.3 ns	± 65.0 ns	0.01440
5th turn	0.27 %	± 60.4 ns	± 65.4 ns	0.01436
6th turn	0.23 %	± 60.5 ns	± 65.8 ns	0.01433

Table 8.3: Muon longitudinal distribution in the Delivery Ring

8.3 Storage Ring Simulations

8.3.1 Simulation of Muon Injection into the Ring

We have developed a model of the injection line and storage ring in order to simulate the injection process. The model is based on routines from the `BMAD` [5] accelerator modeling library. The simulation is a tool for evaluating dependencies on the kicker parameters, (as well as many other beam line and ring parameters). The model includes both the injection line and storage ring. Here we define the injection line as the portion of the beam line extending from the last quadrupole in the M5 line to the good field region of the storage ring dipole as shown in Fig. 8.14.

Just beyond the final M5 quadrupole the muons enter the storage ring through a hole in the backleg iron, emerging between the coils of the ring dipole and finally passing through the superconducting inflector magnet. Muons exit the downstream end of the inflector and enter the good field region of the storage ring. Our model of the storage ring, in addition to the uniform vertical B-field of the dipole, includes the electrostatic quadrupoles, collimators, and of course the kicker magnets. The magnetic field in the hole through the iron and the region from the inside of the backleg iron and through the inflector is based on maps computed with `Opera 3D`. Fig. 8.15 shows the fields along the trajectory of incoming muons.

As the vertical field is increasing in this region, from zero at the edge of the backleg iron, to 1.45T in the gap, the traversing muons experience a very significant horizontal defocusing,

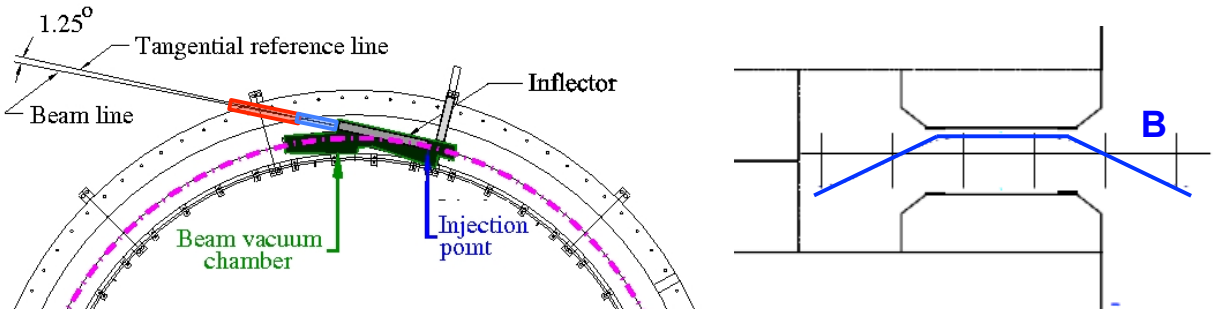

Figure 8.14: (Left) Injection line begins 30 cm upstream of the iron yoke. The hole through the iron is red. The hole through the outer cryostat is blue. Our z-axis is the tangential reference line. (Right) The vertical B-field increases from near zero at the inner edge of the iron to $\sim$ 1.4 T between the poles.

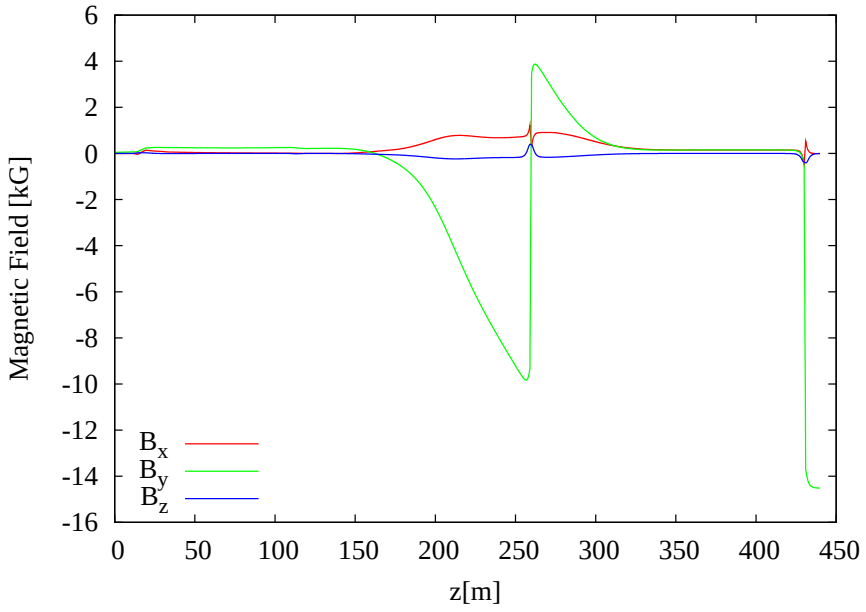

Figure 8.15: Sum of main magnet fringe field and inflector field along the injection line. The origin is 30 cm upstream of the yoke iron. The inflector exit is at 430 cm.

in addition to nonnegligible steering in the horizontal plane. Fig. 8.16 (Left) shows the muon trajectory with initial offset and angle chosen so that the beam exits the inflector tangent to the 7189 mm circle concentric with the closed orbit of the storage ring. The horizontal defocusing is evident in the β-function (Fig. 8.16-Right) propagated along the trajectory in Fig. 8.16(Left). The initial $\beta_{x/y}$ and $\alpha_{x/y}$ just upstream of the hole in the iron are chosen so that there will be a waist with $\beta_x \sim 1.5$ m and $\beta_y \sim 14$ m halfway through the 1.7 m long inflector. These β-values found to yield maximum transmission through the inflector and capture in the storage ring. Note that in order to compensate for the horizontal defocusing of the main dipole fringe field, β_x will necessarily be large in the final quadrupole in the M5 line, and the quadrupole horizontally focusing and as near to the iron as possible.

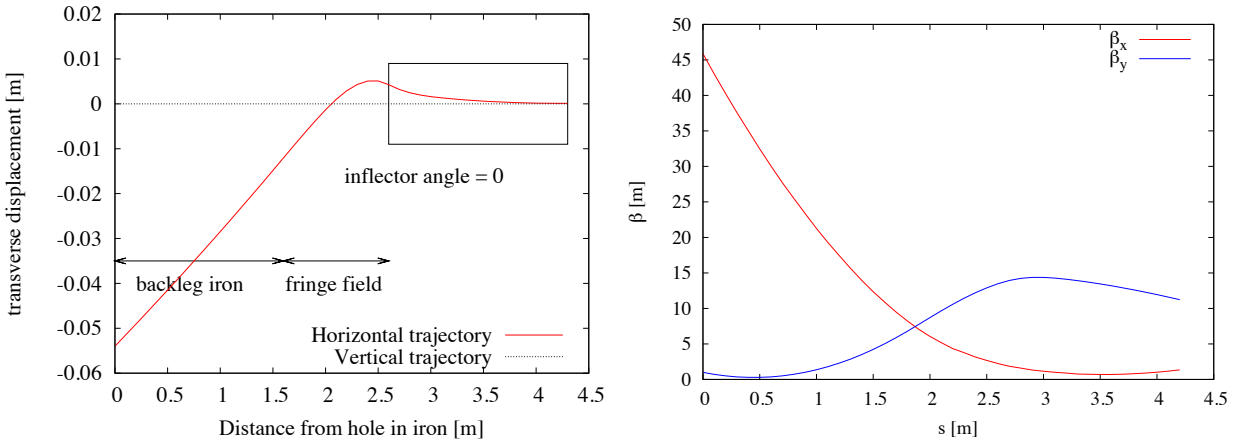

Figure 8.16: (Left) Trajectory through the injection channel. (Right) Horizontal and vertical β-functions with initial values at the upstream end of the line to yield $\alpha_x = \alpha_y \sim 0$ midway through the inflector, and $\beta_x = 1.5$ m. The limiting horizontal aperture is the inflector. The small value of β_x optimizes transmission into the ring. The origin of the coordinate system in these plots is 30 cm upstream of the hole in the magnet iron.

The inflector coils overlap the entrance and exit of the inflector magnet and the phase space volume of the muon beam increases with multiple scattering and energy loss in the coils and cryostat windows.

For the study of capture efficiency we use the muon distribution in the 3D phase space generated by a delta function proton bunch on the conversion target (see Section 8.2.3). A temporal distribution is introduced to correspond with the profile of the incident proton bunch (see Section 7.3.1). The resulting distribution has an emittance $\epsilon_x \equiv \sigma_x \sigma_{px} \sim 11$ mm-mrad, and $\epsilon_y \sim 15$ mm-mrad. The energy spread is $\sim \pm 2\%$ and the length of the bunch $\tau = 120$ ns. Most of the beam fails to get through the injection line. The fraction that does survive is sensitive to

1. Horizontal angle and offset at the entrance to the injection line.

2. Effective β and η in the inflector. The inflector is the limiting aperture. Transmission is optimized when there is a β_x- waist midway through the inflector.

3. Kicker field; overall strength and uniformity.
4. Kicker pulse width, shape and timing.
5. Betatron tunes of storage ring.
6. Storage ring aperture as defined by collimators.
7. Inflector tilt.

We find maximum capture efficiency with the following twiss parameters midway through the inflector $\beta_x = 1.5$ m, $\beta_y = 9$ m and $\eta_x = 0$ m, and $\alpha_x = \alpha_y = \eta'_x = 0$. The incident offset and angle of the injected muons, 30 cm upstream of the hole in the magnet iron, are -5.5 cm and 24 mrad respectively. (The origin of the local coordinate system is the center of the downstream end of the inflector. The z-axis is the perpendicular to the radial line from the center of the storage ring to the center of the inflector aperture. The incident offset and angle are with respect to the z-axis, approximately 4.3 m upstream of the origin.) The optimum kicker field is found to be 200 G. For the purposes of the simulation we assume a kicker pulse with 80 ns flat top and 20 ns rise and fall time. The collimators limit the aperture of the storage ring to a circle with 45 mm radius. The betatron tunes are $Q_x = 0.9264$ and $Q_y = 0.3773$. The closed ring values $\beta_x = 7.99$ m and $\beta_y = 18.43$ m. The chromaticities, that is the energy dependence of the betatron tunes, are $dQ_x/d\delta = -0.104$ and $dQ_y/d\delta = 0.307$ where δ is the fractional energy offset.

The inflector magnet can be rotated (tilted) in the plane of the storage ring about its downstream end by a couple of mrad. This degree of freedom provides some ability to compensate for the fact the net magnetic field in the inflector is non-zero and the muon trajectory is not a straight line. We find best transmission with an inflector tilt angle of $\theta \sim 1.5$ mrad.

Dependence of some of the parameters of the stored beam on the kicker field is shown in Fig. 8.17 (Left), including number of captured muons and the coherent betatron oscillation amplitude of the distribution of stored muons. Fig. 8.17 (Right) shows the dependence on the dispersion at the inflector. If the dispersion is zero there is maximum transmission and capture. The number of muons captured depends very weakly on the dispersion, but the number of muons that are transmitted through the inflector and ultimately lost in the ring falls rapidly with dispersion. Finite dispersion in the inflector will reduce the background in the calorimeters and trackers by reducing the number of muons that will inevitably be lost in the first few turns.

Fig. 8.18 (Left) shows the fate of muons as the distribution proceeds through the fringe fields of the main dipole yoke, the inflector (with its scattering in the end coils and limiting aperture), and finally the fast kicker and around the ring. We find that muons that survive 20 turns in the storage ring are there to stay. Therefore for the purposes of study of dependence of capture efficiency and the like, the capture is defined as survival for 20 turns.

We note that a large fraction of the muon distribution delivered to the storage ring is outside the acceptance of the ring because,

- Temporal extent. The length of the muon bunch is 120 ns. For the purposes of the simulation we have assumed a kicker with 80 ns flattop, thus excluding a significant fraction of the bunch.

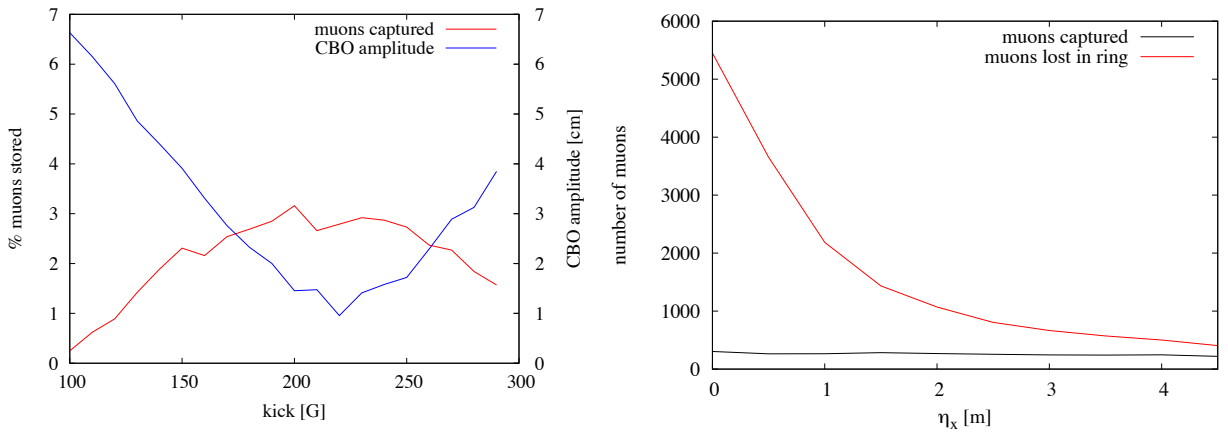

Figure 8.17: (Left) Percentage of muons stored, and amplitude of coherent betatron amplitude of the stored particles versus kicker field. (Right) Number of muons stored and number of muons lost in the ring as a function of dispersion (η_x) in the inflector. The incoming distribution of 10,000 muons is generated and propagated from target to the end of the M5 line. The temporal distribution is taken to correspond to that of the proton bunch.

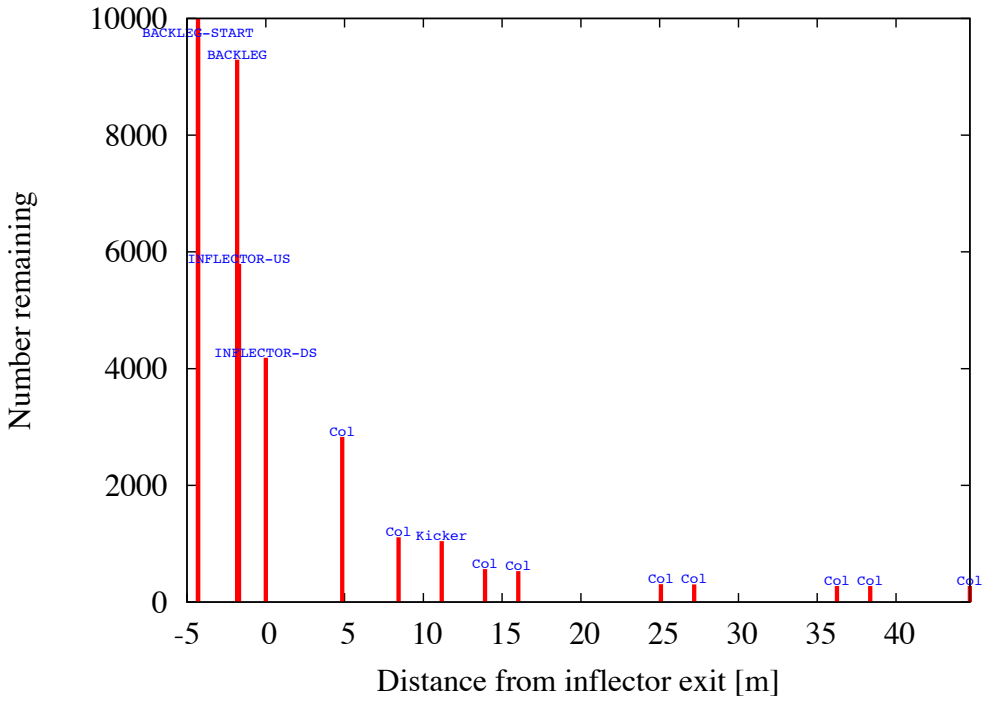

Figure 8.18: Number of muons remaining at points along the injection channel and the first turn around the ring. We find that approximately 80% of the muons that survive the first turn will be stored. The incoming distribution of 10,000 muons is generated and propagated from target to the end of the M5 line. The temporal distribution is taken to correspond to that of the proton bunch.

- Energy spread. The energy width of the distribution is 2% and the energy acceptance of the ring about 0.15%.

Fig. 8.19 shows how the distribution of muons evolves with transport through the injection line and then around the ring. The first of the three plots (Left) shows the horizontal, vertical, energy, and temporal distribution of the distribution projected to conform with the twiss parameters $\beta_x = 1.5$ m, $\beta_y = 9$ m, and $\eta_x = 0$ that are determined to yield maximum capture. Fig. 8.19 (Center) is the distribution of particles after passage through the injection channel including the scattering in the end coils. Particles outside the inflector aperture are lost. Note that when the particles exit the inflector their average horizontal offset is 77 mm. Finally, Fig. 8.19 shows the distribution of muons that survive 20 turns.

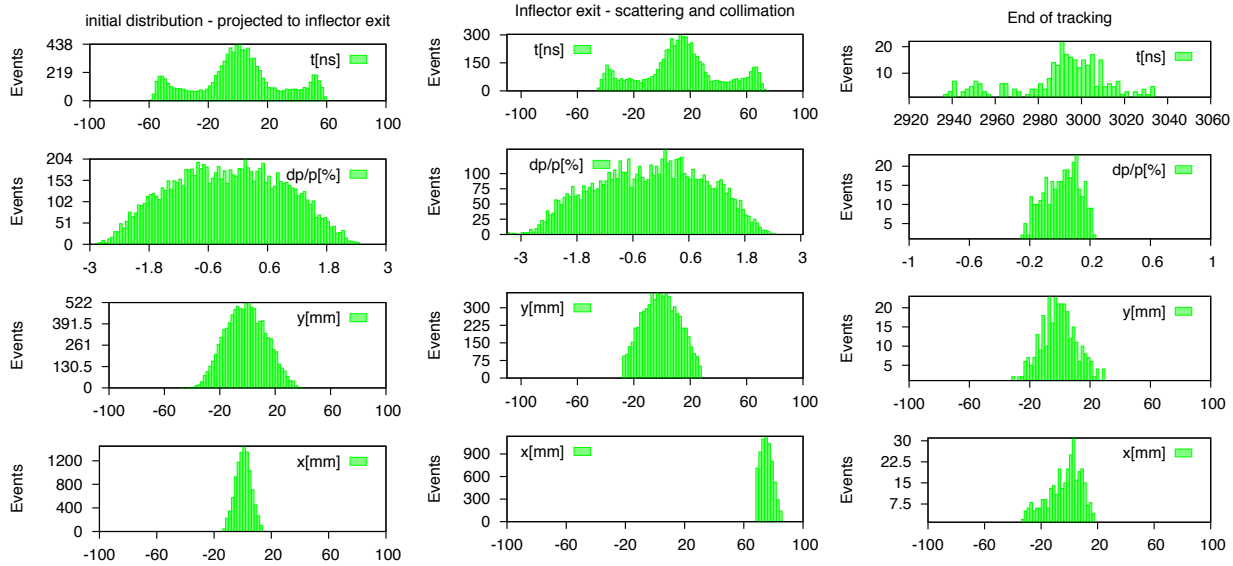

Figure 8.19: (Left) Distribution of of 10,000 muons from pions generated at the target, propagated through the decay line, delivery ring, and M5 line and projected to conform to the twiss parameters ($\beta_x = 1.5$ m, $\beta_y = 9$ m, $\eta_x = 0$) at the inflector exit. The temporal distribution is consistent with the temporal distribution of protons on the conversion target. (Center) Muons that emerge at the inflector exit after propagation through the injection line including scattering in the coil ends. Particles outside the inflector aperture are lost. (Right) Distribution of the 316 muons that survive 20 turns.

8.3.2 Muon Transmission and Storage Simulations

Muon transmission into the ring and the storage fraction are studied using a detailed GEANT4 simulation of the E821 $g-2$ experiment, together with substitutions for certain elements as proposed in this TDR. The storage rate depends strongly on the amount of material the muon beam must traverse, as well as the intrinsic momentum spread (dp/p) of the muon beam. Common to the studies presented here is the assumption that an ideal storage ring kick will be provided to the incoming muon bunch, see Chapter 12. A baseline storage

rate of 6.5% for a 40π mm-mrad muon beam with $|dp/p| < 0.5\%$ is predicted assuming the muon beam must scatter through the two closed ends of the *existing* E821 inflector and the *existing* outer Q1 plate and support. Under an ideal setting of a fully open inflector and no Q1 scattering, a storage of 22% is expected. A summary of a much larger set of studies is presented here.

Simulation Overview

The $g-2$ muon storage region is a torus with central radius 7112 mm and a ± 45 mm inner and outer radius as seen in Fig. 8.20. The $+x$ axis is directed toward the inflector where the muons enter the ring, $+z$ is aimed to the right 90° downstream of the x axis, and the y axis is oriented in and out of the page with the positive direction defined as outward. This coordinate system is useful to describe the ring as a whole (e.g., where is the inflector in relation to some other system), but a different beam-centric coordinate is used when describing beam dynamics. This coordinate system places the muon beam at the origin with the $+x$ direction defined as radially outward, the $+z$ direction aligned with the muon momentum direction or more commonly the azimuth direction in a cylindrical coordinate system, and the y direction remains unchanged from the previous coordinates. This system is shown schematically in Fig. 8.20. The latter coordinate system will be used in this document unless otherwise specified.

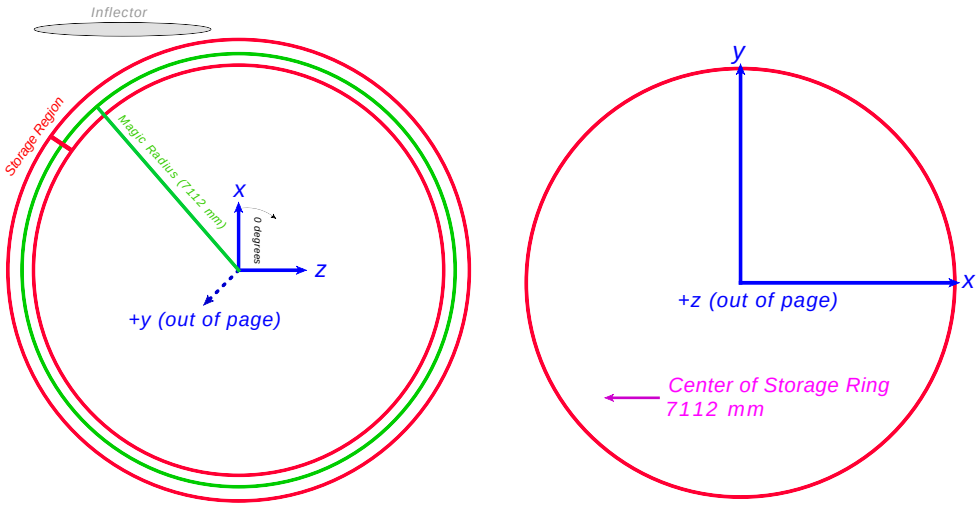

Figure 8.20: Left: Schematic of the $g-2$ muon storage region viewed from above with the associated coordinate system. The magic radius orbit is shown in green and the inner and outer boundaries of the muon storage region are shown in red. The inflector is shown in grey for orientation. Right: Schematic of the muon beam coordinate system viewed head-on inside the $g-2$ storage region

The muon beam used at the start of the simulation is created by an "inflector gun," a `GEANT4` particle gun that allows the user to sample a particle phase space (x, p_x/p_z, y, p_y/p_z) given a set of beam emittances ($\epsilon_{x,y}$) and Twiss parameters ($\alpha_{x,y}$, $\beta_{x,y}$, $\gamma_{x,y}$). The beam

emittance ellipse is defined such that 95% of the beam phase space is contained with the bounded region. This is represented by Eq. 8.1 below, with $x' \equiv p_x/p_z$ and $y' \equiv p_y/p_z$.

$$\gamma_x x^2 + 2\alpha_x x x' + \beta_x (x')^2 < \epsilon_x \tag{8.1}$$
$$\gamma_y y^2 + 2\alpha_y y y' + \beta_y (y')^2 < \epsilon_y \tag{8.2}$$

Only two of the three Twiss parameters are required since the third can be computed using the Courant-Snyder invariant relationship shown in Eq. 8.3. In practice, γ is the derived quantity.

$$\beta\gamma - \alpha^2 = 1 \tag{8.3}$$

Fig. 8.21 is a schematic diagram indicating the relationship between the Twiss parameters and physical degrees of freedom (x, x'). It can be seen in this diagram that the maximum extent of the beam is given by $\sqrt{\varepsilon\beta}$ and the maximum x' is given by $\sqrt{\varepsilon\gamma}$.

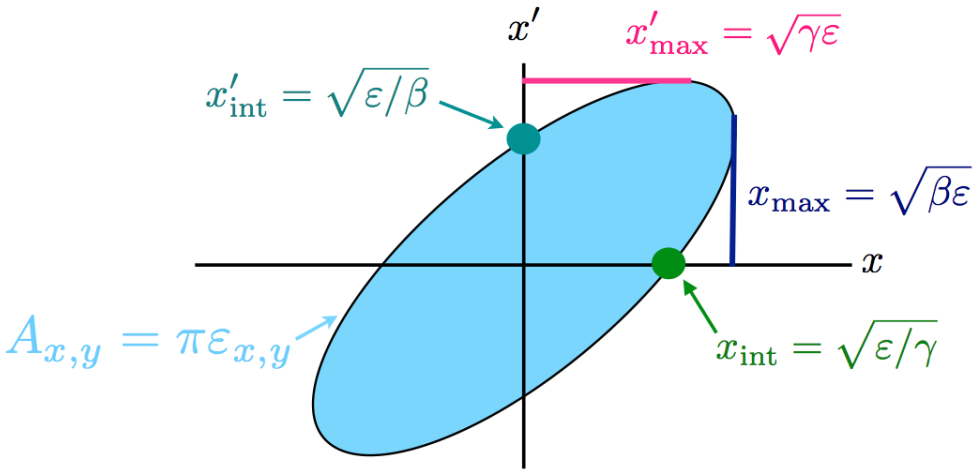

Figure 8.21: Relationship between the Twiss parameters and the physical degrees of freedom x and x'.

The magnitude of the beam momentum is computed by sampling a Gaussian centered at the magic momentum ($p_{\text{m}} \equiv m_\mu/a_\mu = 3.094$ GeV/c) and a width (dp/p). Typical values for $|dp/p|$ range between 10^{-4} and 10^{-1} for this study.

The beam is generated at a fixed z position either along the inflector main axis or along the azimuthal direction within the $g-2$ storage region. Typically, the Twiss parameters are defined at the "downstream" end of the inflector one millimeter before the beam must traverse inflector coils. A transport matrix is employed to recompute the Twiss parameters when the beam originates at the "upstream" end of the inflector, which is defined as one millimeter before the beam must enter the outer inflector cryostat. A drift space approximation is used for the transport matrix. In all studies, the muon storage is computed as the ratio of muons remaining in the ring after 100 revolutions vs. the incoming flux, with muon decay turned off. The storage ring kicker magnetic field is assumed to be a square pulse applied to the first turn only, and at an ideal magnitude (typically 220 G), tuned to

maximize the storage rate for the given conditions. The E821 LCR pulse was also studied for comparison. This non-ideal pulse shape (and magnitude) were not considered for E989. Variations studied and optimized in the following include the beam entrance "launch" angle into the inflector, the geometrical inflector angle with respect to a tangent to the storage ring central radius, and the momentum spread $|dp/p|$ of the incoming beam. Here we report only on the storage rate for $|dp/p| < 0.5\%$; the intrinsic momentum acceptance of the ring is much smaller.

A number of discrete variations were explored. They include:

- **Inflector Field:** *Mapped* means the computed, true inflector magnetic field is loaded and vectorially added to the main magnet fringe field. *Vanish* means the field within the inflector is identically zero (idealized).

- **Inflector Geometry:** *Closed-Closed* represents the existing E821 inflector with the magnetic coils covering both the upstream and downstream ends. It also includes the aluminum cryostat materials. *Open-Open* is a hypothetical new inflector with both upstream and downstream ends open. Intermediate cases have also been studied.

- **Quad Geometry:** *Full* is the existing E821 geometry for the outer Q1 quadrupole plate and the mechanical Macor standoffs that hold the plate in position. The trajectory of the incoming muon beam passes through these materials at a small glancing angle. The energy loss and multiple scattering have an impact on the storage fraction. *No Quads* represents the proposed E989 geometry where the Q1 outer plate is displaced radially such that no muons pass through these materials. Intermediate geometries—e.g., existing Q1 and removed standoffs—were also studied.

- **Incoming Beam Tune:** *The E821-match* parameters were determined by minimizing the beam amplitude within the inflector volume. *Ideal-match* parameters are derived by assuming ideal phase space matching into the storage ring with uniform quadrupole coverage.

The generated phase space for an $A = \epsilon\pi = 40\pi$ mm-mrad beam starting in the Downstream position with the two beam types, E821-match and Ideal-match, are shown in Fig. 8.22.

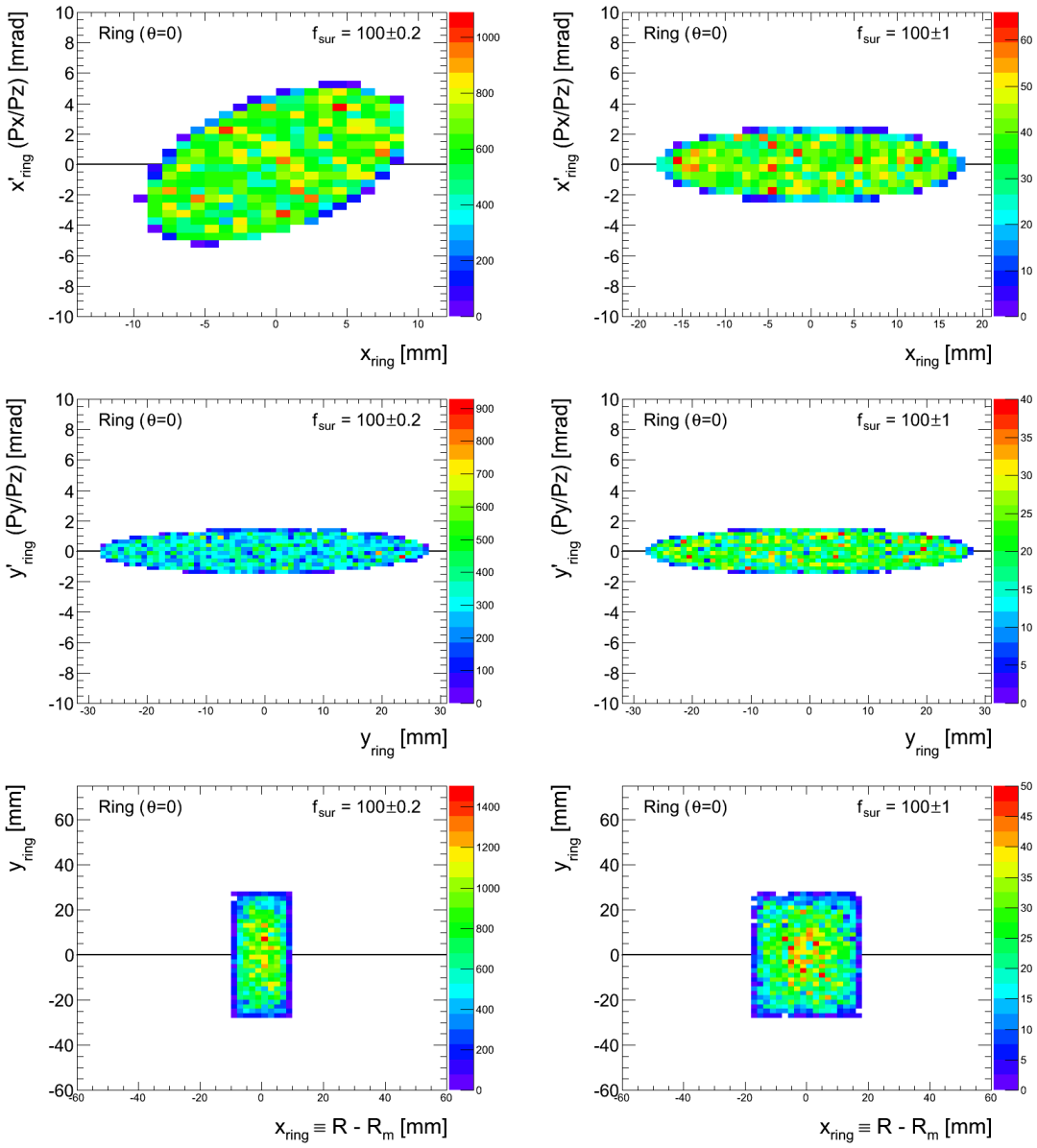

Figure 8.22: Generated Phase Space for the E821-match (left column) and Ideal-match (right column) Beams. The left column shows $x - x'$ and the right column shows $y - y'$. In all plots the origin intersects with the main inflector axis. The most noticeable difference between these two beams is the horizontal width.

Results for Beam Starting at Upstream Entrance of the Inflector

Here we present the main findings of the studies in which the incoming beam is launched into the upstream entrance of the inflector. It must cross both ends of the inflector (whether "open" or "closed," through the 1.7 m "D"-shaped inflector beam channel physical limitations, and through, if applicable, the outer Q1 plate/support system before entering the storage region. Fig. 8.23 is a schematic of the magic radius (red line) and the starting location of the muon momentum vector (blue arrow) and their relationship to other systems in the ring. The region indicated by "Kicker Plates" provides the idealized horizontal deflection appropriate to the given situation. There are two degrees of freedom, δ and ℓ, as the beam enters the storage region. If the inflector is oriented such that it is tangent to the ring, then the maximum storage rate occurs when $\ell = 0$ and $\delta = -6$ mrad in the case of a fully vanishing magnetic field within the inflector. In the case of a fully mapped magnetic field, the optimal inflector angle δ is between $[-2, -4]$ mrad and the optimal launch angle ℓ is between $[-12, -14]$ mrad.

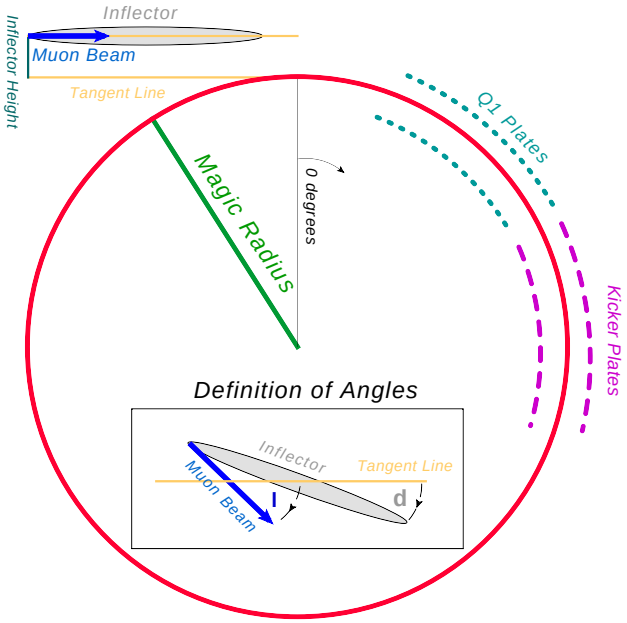

Figure 8.23: Schematic of the $g-2$ storage ring as viewed from above. The starting location of the muon momentum vector in relation to the magic radius and other detector elements is shown by the blue arrow. The beam originates at the inflector entrance.

The muon storage fraction approaches a maximum when the inflector is fully open and the outer Q1 plate and support are massless only for the E821-match beam tune. The Ideal-match beam storage rates are noticeably lower than the E821-match because more of the beam is lost while traversing the inflector beam channel. Similarly, closing the inflector will drop the storage rate by approximately a factor of two and is nearly equivalent to making the Q1 plate and support massless. Fig. 8.24 shows curves of storage fraction for several benchmark scenarios of inflector and Q1 plate/support geometries. The plots show the fraction vs. the momentum width of the incoming beam, assuming the beam flux is *common*

for all scenarios; thus, the fraction is reduced as the beam width increases. It is instructive to compare performance at the common $|dp/p| < 0.5\%$ point to tie into the calculation of the muon flux described in Section 8.2.3. Table 8.4 shows the storage rate for the two inflector geometry options combined with the two Q1 geometries for the E821-match beam with $|dp/p| < 0.5\%$.

Table 8.4: Muon Storage Rates in % for 4 combinations of inflector and Q1 geometries for an E821-match muon beam with $|dp/p| < 0.5\%$. The underlined value for the open inflector and massless quads represents the maximum storage fraction obtainable for an incoming beam having $|dp/p| < 0.5\%$. The bold entry for closed inflector, massless quads represents the best estimate of the starting geometry for E989, prior to installation of a new inflector. All statistical uncertainties are well below 0.1%

Q1 Geometry → Inflector Geometry ↓	Massless Q1 Plate and Support	Massive Q1 Plate and Support
Fully Open	<u>22.0</u>	13.0
Fully Closed	**10.0**	6.5

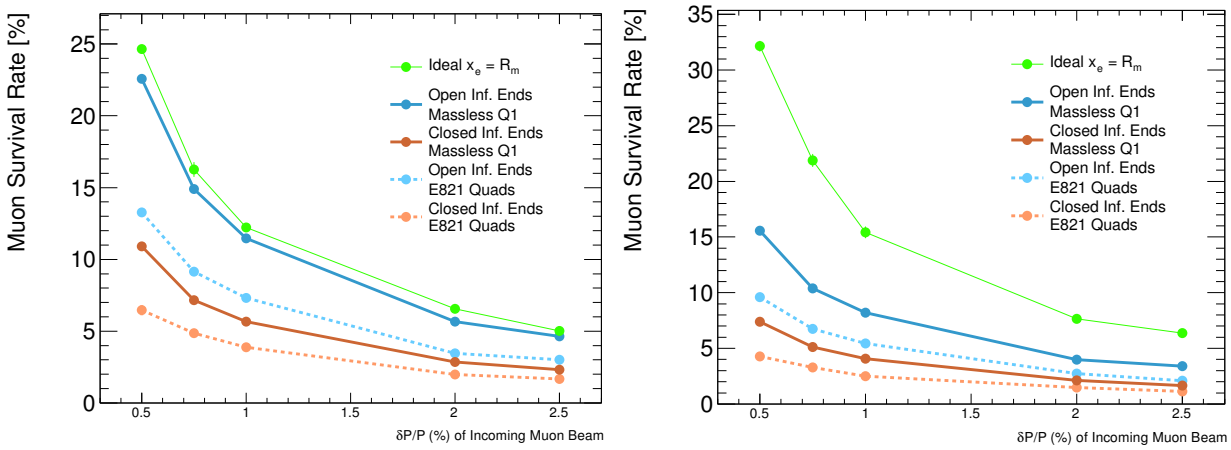

Figure 8.24: Comparison of the muon storage rates for a wide range of dp/p with a variation of inflector and outer Q1 plate/support geometries assuming $A = 40\pi$ mm-mrad beam with the E821-inflector Twiss parameters (left) and the Ideal-match beam parameters (right). The "Ideal" entry represents a pencil beam launched at the magic radius inside the storage ring.

8.4 Summary

Using a sequence of specialized tools we developed a software model of the $(g-2)$ beamline, which allow us study various aspects of the beam transport and delivery for the E989 muon $(g-2)$ experiment at Fermilab. A complete "end-to-end" simulation has been performed to

estimate the number of stored muons per proton on target, generate the expected distributions of stored muons, estimate the polarization of the muon beam and build a foundation for future systematic studies. Using the software models, we performed optimization studies of pion capture by the lithium lens, muon capture by the decay line, beam injection and transmission into the $(g-2)$ storage ring. According to our simulations, we expect to have approximately 8.1×10^{-7} muons per proton on target at the end of the beamline (at the entrance into the $(g-2)$ inflector) with $\Delta p/p_{\text{magic}} \approx 1.2\%$ RMS. Assuming baseline design parameters of the inflector, quadrupole Q1 and muon kicker, we expect to store approximately 2×10^{-8} muons per proton on target in the $(g-2)$ storage ring. The polarization of the stored muons is about 95%.

As with any simulation, especially of a system that has not yet been built, these estimates can only yield expectations of performance and provide guidance going forward. Many effects have yet to be included into the simulations, such as random misalignment errors and powering/setting errors as set by the expected tolerances, though work will continue on these fronts and others. However there will always be unknown sources of errors, particle loss, emittance growth, etc., which can lead to a reduction in overall particle transmission. The beam line systems being developed at Fermilab for $(g-2)$ are flexible enough to provide many options for further optimization of beam performance after commissioning. The tact taken in the end-to-end simulation has been to create a modeling system that is as flexible as possible to adequately simulate the as-built system and to allow further modeling developments throughout the life of the experiment as more details of the beam delivery system are understood.

References

[1] N.V. Mokhov, "The MARS Code System User's Guide", Fermilab-FN-628 (1995); N.V. Mokhov, O.E. Krivosheev, "MARS Code Status", Proc. Monte Carlo 2000 Conf., p. 943, Lisbon, October 23-26, 2000; Fermilab-Conf-00/181 (2000); N.V. Mokhov, "Status of MARS Code", Fermilab-Conf-03/053 (2003); N.V. Mokhov, K.K. Gudima, C.C. James *et al.*, "Recent Enhancements to the MARS15 Code", Fermilab-Conf-04/053 (2004); `http://www-ap.fnal.gov/MARS/`. MARS was developed in part with Government funding provided under DOE Contract DE-AC02-76CH03000.

[2] V. Tishchenko *et al.*, "Optimization of the E989 pion capture", E989 note #1591, `http://gm2-docdb.fnal.gov:8080/cgi-bin/ShowDocument?docid=1591`.

[3] J. Johnstone, "M2, M3 and Ring MAD8 Lattice Files 05.10.2013", E989 note #700, `http://gm2-docdb.fnal.gov:8080/cgi-bin/ShowDocument?docid=700`.

[4] C. Yoshikawa *et al.*, "Optimization of the Target Subsystem for the New $g-2$ Experiment", IPAC2012.

[5] D. Sagan, Nucl. Instrum. Methods Phys. Res. A558, 356 (2006).

[6] `MAD8`, `http://hansg.home.cern.ch/hansg/mad/mad8/mad8.html`.